LEGO-MIMO Architecture: A Universal Multi-Input Multi-Output (MIMO) Power Converter with Linear Extendable Group Operated (LEGO) Power Bricks

Yenan Chen, Ping Wang, Youssef Elasser and Minjie Chen
Princeton University, Princeton, NJ 08540, USA
Email: {yenanc, pwang2, yelasser, minjie}@princeton.edu

***Abstract*—This paper presents the design and implementation of a universal Multi-Input Multi-Output (MIMO) power converter with many Linear Extendable Group Operated (LEGO) building blocks, namely LEGO-MIMO architecture. The LEGO-MIMO architecture can be used to synthesize a wide range of power converters with universal input and output range. In a LEGO-MIMO design, multiple dc-ac units are coupled together through a multi-winding transformer. Each dc-ac unit can individually regulate its port voltage and power. Many dc-ac units can be connected in series or parallel to meet the targeted voltage or current ratings. The modular units can be designed and manufactured in large volume with low cost. This paper studied the design methods for the multi-winding transformer. We also investigated the strategy to control the sophisticated power flow in the multi-winding transformer and proposed a matrix model for the LEGO-MIMO converter with reduced order to simplify the control algorithm. A LEGO-MIMO prototype with 12 LEGO bricks and a 12-winding transformer has been built and tested to verify the effectiveness of the proposed LEGO-MIMO architecture.**

***Index Terms*—power electronics building block, dc-dc conversion, multiport power converter, multi-winding transformer.**

I. Introduction

The demand of multiport power conversion is rapidly increasing in many power conversion applications such as 1) solar power generation systems [1], [2]; 2) uninterrupted power supply with multiple energy sources [3]; 3) battery management system [4]; 4) server racks [5] which have a large number of modular cells need to be connected in series and/or parallel and need be coordinated to achieve maximum system performance and safety operation. There are two major categories of multiport power conversion architectures: dc-coupled architecture and ac-coupled architecture. As compared in Fig. 1, in a multiport dc-coupled architecture, each source/load unit is connected to a dc-link capacitor through a standalone dc-dc isolated converter with an internal "dc-ac-dc" power conversion stage or a dc-dc non-isolated converter. Each dc-dc converter has a single input and a single output. Essentially the dc-coupled architecture is the combination of several conventional dc-dc converters. Due to the existence of the dc-link capacitor, the power flow is decoupled and can be easily modulated by controlling each independent dc-dc converter. In a multiport ac-coupled architecture, each source/load unit is connected to an ac-link (usually a multi-winding transformer) through a dc-ac converter, which has only one "dc-ac" power conversion stage. Many sources and loads are connected together by a single core and multiple windings. The ac-coupled architecture offers higher efficiency and lower component count, but requires precise magnetics models and advanced power flow control methods [6].

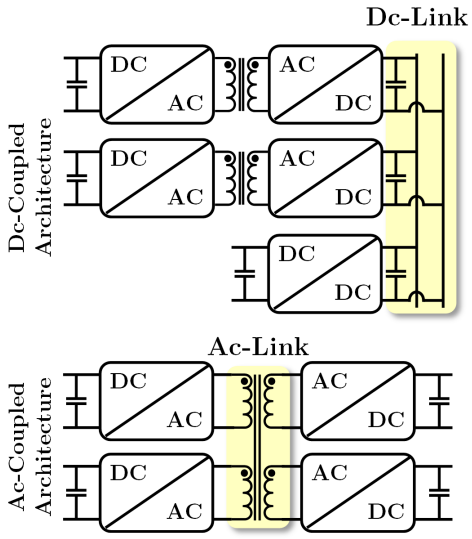

Fig. 1. Multiport dc-coupled architecture and multiport ac-coupled architecture. The multiport ac-coupled architecture has lower component count and reduced power conversion stress, but requires more precise magnetic models and more sophisticated power flow control strategy.

The concept of connecting many dc-ac ports with a multi-winding transformer has been previously explored. The magnetic design is important to improve the efficiency and power density. [7] proposed a matrix transformer structure to integrate four transformers into one magnetic core with reduced core loss. A novel "Snake-Core" transformer structure was introduced in [8], which maintains current sharing in multiple parallel connected secondary windings to reduce the conduction loss. For multiport power converters, the voltage and current rating of each port usually have a wide range, which require different components selection, magnetic structure and insulation distance. For most existing designs, the winding turns and converter components are customized according to the specification of each port. The basic dc-ac ports cannot be simply reused in new designs with different ratings.

One way to mitigate the challenge of designing a universal power converter topology is using the standard modules or power electronics building blocks (PEBB) [9]. A *Linear Ex-*

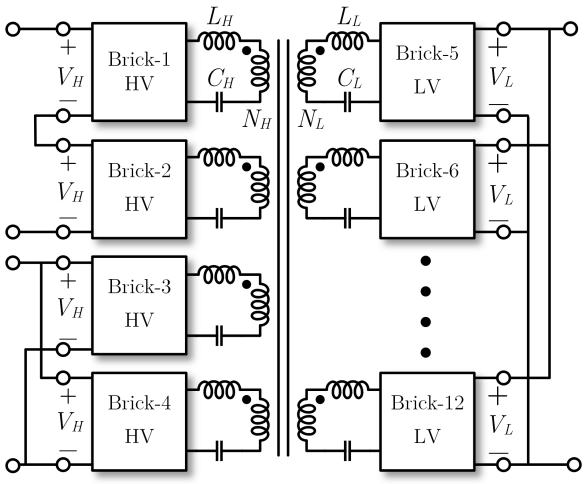

Fig. 2. An example multiport system with LEGO-MIMO architecture. A large number of HV and LV bricks can be connected in series or parallel to create input/output ports with highly flexible voltage and power ratings.

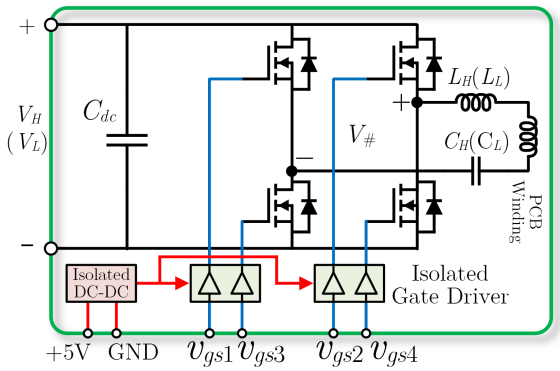

Fig. 3. Circuit schematic of the LEGO power brick including a power stage and a control stage. Both the power stage and the control stage are highly modular to enable "plug-and-play" extensions and reconfigurations.

tendable Group Operated (LEGO) design concept is explored in this paper to reuse the building blocks in a variety of different applications by series and parallel reconfiguration of building blocks. As one type of PEBB, the LEGO concept incorporates the standard power conversion hardware unit and a plug-and-play architecture, featuring flexible configuration, adjustable operation range and low packaging cost. With the proposed LEGO concept, the port power and voltage of multiport converter can be simply extended by paralleling or cascading multiple power bricks. The power bricks belonging to the same port are group operated by the same gate drive signals for plug-and-play operation. In this paper, we introduced the hardware design of the LEGO bricks in an example MIMO converter with a single magnetic core and reconfigurable inputs and outputs. The optimization of the multi-winding transformer is presented and a reduced order inductance matrix is proposed to simplify the sophisticated power flow control in the multiport converter. The design concepts and theoretical derivations are verified by experimental results.

The remainder of this paper is organized as follows: Section II introduces the circuit topology of the LEGO-MIMO architecture and its operation principles. Section III presents the control strategy of the LEGO-MIMO architecture. Section IV presents the design methods for the multi-winding magnetics with finite element analysis (FEA) and reduced-order modeling. Experimental results of a prototype MIMO converter with 12 LEGO power bricks is summarized in Section V. Finally, Section VI concludes the paper.

II. MIMO Converter with LEGO Power Bricks

Fig. 2 shows the schematic of a LEGO-MIMO architecture with 12 modular bricks. Two types of LEGO bricks are included: four high-voltage (HV) bricks and eight low-voltage (LV) bricks. The HV bricks can be stacked in series to interface with high voltage ports (e.g., 400V dc bus with PFC), and the LV bricks can be connected in parallel to interface with high current ports (e.g., a 12V, 20A port as needed for point-of-load converters). The inputs and outputs of the MIMO converter are also reconfigurable by reconnecting the LEGO bricks. For all the LEGO bricks in the same port, the dc bus voltage and brick power are equal (V_H for all HV bricks and V_L for all LV bricks) so that the port voltage and port power can be linearly extended by adding more LEGO bricks.

The power stage and control stage of the LEGO power brick are designed for this purpose. Fig. 3 shows the schematic of a LEGO power brick, comprising one full-bridge circuit with isolated gate drivers and isolated auxiliary power supply, the dc bus capacitor C_{dc}, a branch inductor (L_H for HV bricks and L_L for LV bricks), a dc blocking capacitor (C_H and C_L), and a PCB winding with turns number of N_H or N_L. All LEGO bricks are interconnected by a single magnetic core. The two phase arms of the full-bridge converter are controlled by complementary gate drive signals with duty ratio of 50%. Similar to the dual-active bridge (DAB) converter, all the LEGO bricks are modulated by phase-shift control with trapezoidal current in the branch inductors.

Fig. 4 shows the "group control" diagram for the LEGO power bricks. One port can include an arbitrary number of LEGO bricks but only needs one group of gate drive signals. The group control strategy enables the "plug and play" function for the LEGO-MIMO architecture. In other words, the controller only senses the port voltage and/or port current for feedback control. There is no control effort to balance the dc bus voltage of series-stacked LEGO bricks and equalize the output current of each parallel-connected LEGO bricks. The voltage balancing and current sharing of the LEGO-MIMO architecture can be guaranteed by proper magnetic design and passive impedance matching.

III. Power Flow in LEGO-MIMO Architecture

As shown in Fig. 5, the full-bridge converters of LEGO bricks can be modeled as square wave voltage sources $V_{\#1}$–$V_{\#k}$ which drive the multi-winding transformer with a single flux linkage. In the cantilever model shown Fig. 5, the interconnection of the multiple windings can be represented by a network of equivalent inductance L_{ij} linking Brick i and Brick j [10], and the equivalent ground inductance L_{Gi}. The

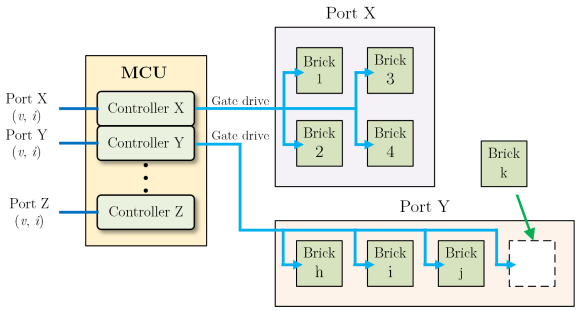

Fig. 4. Principles of the group control strategy for the LEGO-MIMO architecture. Modular bricks can be plugged in without changing the overall control strategy. The system is "linearly extendable" with voltage balancing and current sharing.

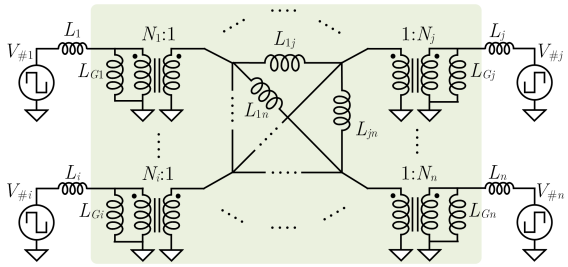

Fig. 5. LEGO bricks and the cantilever model of a multi-winding transformer.

dc blocking capacitors are neglected in this model due to their small impedance. Following the principles of multi-active-bridge (MAB) converter [5], the average power delivered to Brick i from the transformer is:

$$P_i = \frac{N_i V_i}{2\pi^2 f_s} \sum_{j \neq i} \frac{N_j V_j (\Phi_i - \Phi_j)\left(\pi - |\Phi_i - \Phi_j|\right)}{\left(N_i^2 N_j^2 L_{ij} + N_j^2 L_i + N_i^2 L_j\right)}. \quad (1)$$

Here Φ_i and Φ_j are the phase-shift angles of Brick i and Brick j; L_i and L_j are the external branch inductors (L_H and L_L in Fig. 3); N_i, N_j are the turns number; V_i, V_j are the dc bus voltage of LEGO bricks; f_s is the switching frequency.

The small signal model for the dc bus voltage of the total n LEGO bricks in the LEGO-MIMO converter is [5], [11]:

$$\hat{\boldsymbol{v}} = \boldsymbol{G_v}\hat{\boldsymbol{v}} + \boldsymbol{G_\phi}\hat{\boldsymbol{\phi}}. \quad (2)$$

Here $\boldsymbol{G_v}$ is the the small signal transfer matrix from the bus voltage perturbations of other bricks. $\boldsymbol{G_\phi}$ is the small signal transfer matrix from phase-shift perturbations to the dc bus voltage of LEGO brick. Both $\boldsymbol{G_v}$ and $\boldsymbol{G_\phi}$ require the load impedance of each LEGO brick.

However, this small signal model is not suitable for the LEGO-MIMO architecture. As mentioned in Section II, if many LEGO bricks are connected in series or parallel, the load impedance of each LEGO brick can not be directly obtained in a port with multiple parallel or stacked bricks. The small signal matrix becomes over complicated when the LEGO-MIMO converter has a large number of bricks.

A matrix reduction method is developed to analyze the small signal model of the LEGO-MIMO architecture with sophisticated series-parallel configurations. The winding voltage and

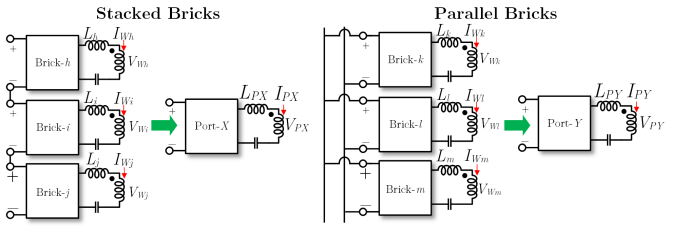

Fig. 6. Equivalent circuits of series bricks and parallel bricks in one port.

current in an n-winding transformer can be described as an $n \times n$ impedance matrix:

$$\begin{bmatrix} V_{W1} \\ \vdots \\ V_{Wn} \end{bmatrix} = j\omega \begin{bmatrix} L_{11} & \cdots & M_{1n} \\ \vdots & \ddots & \vdots \\ M_{n1} & \cdots & L_{nn} \end{bmatrix} \begin{bmatrix} I_{W1} \\ \vdots \\ I_{Wn} \end{bmatrix}, \quad (3)$$

where V_{Wi} is the winding voltage, I_{Wi} is the winding current, L_{ii} is the self-inductance of Winding i, $M_{ij} = M_{ji}$ are the mutual-inductance between Winding i and Winding j. The self-inductance and mutual-inductance can be exacted by analytical model, experimental measurements, or FEA simulations. The winding resistance is neglected.

Fig. 6 shows the equivalent circuit model of the stacked bricks in Port X and parallel bricks in Port Y. The equivalent winding voltage of Port X is the summation of winding voltage of each stacked brick:

$$V_{PX} = V_{Wh} + V_{Wi} + V_{Wj} + \cdots. \quad (4)$$

Since Brick h to Brick j are modulated in phase with the same group of gate drive signals, we can assume that the winding current in every brick of Port X are equal:

$$I_{PX} = I_{Wh} = I_{Wi} = I_{Wj} = \cdots. \quad (5)$$

The equivalent external branch inductance L_{PX} is the summation of the series inductance of all brick branch inductors:

$$L_{PX} = L_{Wh} + L_{Wi} + L_{Wj} + \cdots. \quad (6)$$

For Port Y with parallel LEGO bricks, the equivalent winding voltage equals the winding voltage of every brick:

$$V_{PY} = V_{Wk} = V_{Wl} = V_{Wm} = \cdots. \quad (7)$$

The equivalent winding current is the summation of all the individual brick winding currents:

$$I_{PY} = I_{Wk} + I_{Wl} + I_{Wm} + \cdots. \quad (8)$$

The equivalent branch inductance equals to the parallel inductance of all brick branch inductors:

$$L_{PY} = L_{Wk} || L_{Wl} || L_{Wm} || \cdots. \quad (9)$$

Suppose the total n LEGO bricks are divided into m ports ($m \leq n$), the voltage conversion matrix $\boldsymbol{Q_V}$ converts the voltage of each brick winding into the voltage of each equivalent port winding:

$$\begin{bmatrix} V_{P1} \\ \vdots \\ V_{Pm} \end{bmatrix} = \begin{bmatrix} Q_{V11} & \cdots & Q_{V1n} \\ \vdots & \ddots & \vdots \\ Q_{Vm1} & \cdots & Q_{Vmn} \end{bmatrix}_{m \times n} \begin{bmatrix} V_{W1} \\ \vdots \\ V_{Wn} \end{bmatrix}. \quad (10)$$

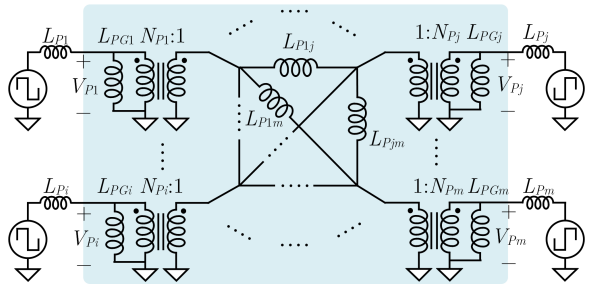

Fig. 7. LEGO bricks and a simplified cantilever model with m windings which can be used to model the large-signal and small-signal dynamic behaviors of the system.

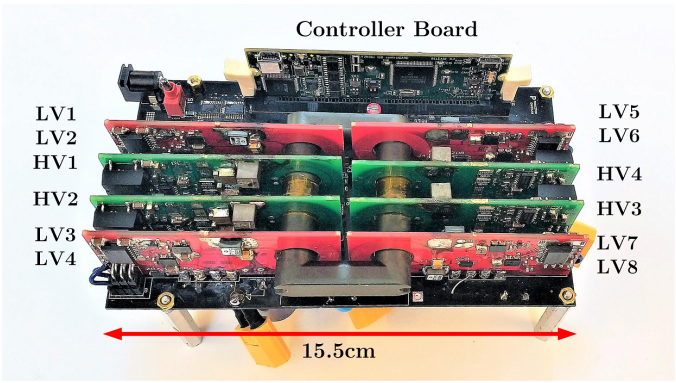

Fig. 8. A 500W LEGO-MIMO converter with 12 LEGO bricks, including 4 HV bricks (green) and 8 LV bricks (red) with interleaved winding structure.

Each element of $\boldsymbol{Q_V}$ can be found by:

- if Port i consists series-connected bricks, and Brick j belongs to Port i, then $Q_{Vij} = 1$; Otherwise, $Q_{Vij} = 0$.
- if Port i consists parallel-connected bricks, and Brick j, k, l belong to Port i, then set any one of Q_{Vij}, Q_{Vik} or Q_{Vil} be 1, and all other $Q_{Vi?}$ on the same row as 0.

The equivalent port winding current can be extracted by current conversion matrix $\boldsymbol{Q_C}$ with the similar rules:

$$\begin{bmatrix} I_{W1} \\ \vdots \\ I_{Wm} \end{bmatrix} = \begin{bmatrix} Q_{C11} & \cdots & Q_{C1m} \\ \vdots & \ddots & \vdots \\ Q_{Cn1} & \cdots & Q_{Cnm} \end{bmatrix}_{n\times m} \begin{bmatrix} I_{P1} \\ \vdots \\ I_{Pn} \end{bmatrix}. \quad (11)$$

Each element of $\boldsymbol{Q_C}$ can be found by:

- if Brick i belongs to a series-connected Port j, then $Q_{Cij} = 1$; Otherwise $Q_{Cij} = 0$.
- if Brick i, k, l belong to a parallel-connected Port j, then set $Q_{Vij} + Q_{Vkj} + Q_{Vlj} = 1$.

The $m \times m$ "port-to-port" impedance matrix $\boldsymbol{M_{P2P}}$ is:

$$\boldsymbol{M_{P2P}} = \boldsymbol{Q_V} \boldsymbol{M_{W2W}} \boldsymbol{Q_C}. \quad (12)$$

where $\boldsymbol{M_{W2W}}$ is the $n \times n$ impedance matrix in (3).

If one port has both series-connected bricks and parallel-connected bricks. The matrix conversion can be performed in two steps: firstly converting the port to several sub-ports with series-connected bricks; then converting these parallel-connected sub-ports to one port.

With the $m \times m$ impedance matrix, the n-winding transformer can be simplified to a cantilever model with m-equivalent windings as shown in Fig. 7. N_{Pi} is the equivalent turns number, which equals to the total turns number of series-connected bricks and the identical turns number of parallel-connected bricks. Based on the simplified cantilever model, the equivalent winding voltages and winding currents can be linked by the equivalent inductance linking different ports:

$$\boldsymbol{I_P} = \boldsymbol{M_{V2C}} \boldsymbol{V_P}. \quad (13)$$

Here $\boldsymbol{I_P}$ and $\boldsymbol{V_P}$ are the equivalent winding current matrix and voltage matrix. $\boldsymbol{M_{V2C}}$ is the admittance matrix linking winding voltage with winding current:

$$\boldsymbol{M_{V2C}} = \frac{1}{j\omega} \begin{bmatrix} Y_{11} & \cdots & Y_{1m} \\ \vdots & \ddots & \vdots \\ Y_{m1} & \cdots & Y_{mm} \end{bmatrix}, \quad (14)$$

$$Y_{ii} = \frac{1}{L_{PGi}} + \frac{1}{N_{Pi}^2} \sum_{j \neq i} \frac{1}{L_{Pij}}, Y_{ij} = \frac{-1}{N_{Pi} N_{Pj} L_{Pij}}. \quad (15)$$

This admittance matrix is the inverse of the "port-to-port" impedance matrix:

$$\boldsymbol{M_{V2C}} = \boldsymbol{M_{P2P}^{-1}}. \quad (16)$$

All parameters in the simplified cantilever model can be obtained from (16). Substituting them into (1) and replacing the brick voltage with port voltage gives the average power delivered to Port i from the other ports. For example, in the MIMO converter with 12 LEGO bricks, the small signal transfer matrices of the brick bus voltage $\boldsymbol{G_v}$ and $\boldsymbol{G_\phi}$ are both 12×12 matrices. With the matrix conversion, the small signal transfer matrices are simplified to 4×4 matrices (with 4 input and output ports), which significantly mitigates the control complexity. The phase-shift feedback control and time-sharing control introduced in [11] can be similarly applied to the LEGO-MIMO converter.

IV. Multi-winding Transformer Design

Fig. 8 shows the prototype MIMO converter including 8 modular PCB boards, one UU type magnetic core, one mother board and one controller board. One modular PCB board has one HV LEGO brick or two LV LEGO bricks. There are 4 HV bricks and 8 LV bricks in total in this prototype. The UU core is installed through the central cutout holes of the PCB windings, which couples all the HV bricks and LV bricks together. The mother board connects the LEGO bricks in series or in parallel as group operated ports. The key parameters of the LEGO-MIMO converter are listed in Table I.

There are many ways of placing the HV and LV bricks around the magnetic core. Two winding structures are investigated and compared in this paper. Fig. 9 shows the cross-section view of the two winding structures - one interleaved, and the other non-interleaved. The HV bricks are labeled in green and the LV bricks are labeled in red. Since the modular PCB board is manufactured with 4-layer copper foils, the 1-turn winding of the LV brick is divided into two parallel-connected copper layers. Suppose all the HV bricks are on the primary side and all the LV bricks are on the secondary side, the primary current I_p and secondary current I_s in the

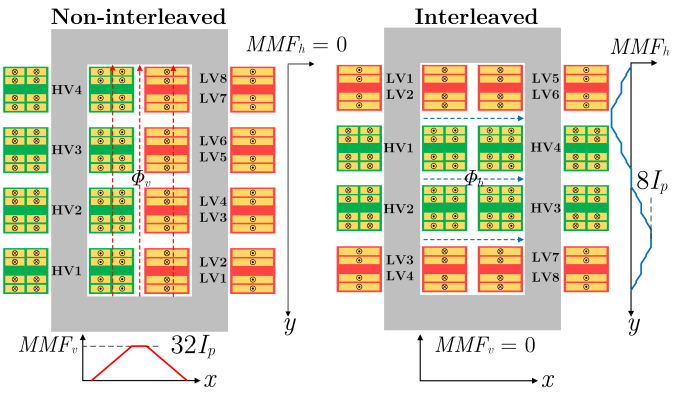

Fig. 9. Winding cross-section view and MMF distribution in an ideal multi-winding transformer with infinite permeability and high coupling coefficient.

multiple windings of this multi-winding transformer with an ungapped infinite permeability core satisfy:

$$32 \times I_p = 16 \times \frac{1}{2} \times I_s. \tag{17}$$

Fig. 9 also shows the magnetomotive force (MMF) in this multi-winding transformer with interleaved and non-interleaved winding structures. In the non-interleaved structure, the horizontal flux Φ_h is canceled by the same winding current of two adjacent HV or LV windings and the MMF at the same position of the window area is zero, which can relief the proximity effect on the top and bottom surface of the PCB coppers. However, the opposite currents of one HV brick on the left side and one LV brick on the right side enhance the vertical flux Φ_v and the maximum MMF is $32I_p$ at the central vertical axis of the window area, which will induce eddy current at the side surface of PCB coppers.

In the interleaved structure, the flux and MMF distribution are very different from those in the non-interleaved structure. The horizontal flux in the window area is enhanced while the vertical flux is canceled. The maximum MMF is $8I_p$ at the gap between one HV brick and one LV brick. The proximity effect on the side surface of the PCB windings is reduced while eddy current will be induced on the top surface of PCB board on the 2^{nd} and 4^{th} row (HV1, HV4, LV3, LV7), and the bottom surface of PCB board on the 1^{st} and 3^{rd} row (LV2, LV6, HV2, HV3).

For a practical magnetic core with a permeability of μ_r, the MMF on the left pillar with non-interleaved winding structure is $32I_p$, while it is $16I_p - 4I_s$ with interleaved winding structure. Both the magnetic field strength and the core loss are reduced with interleaved winding structure.

The copper thickness is 70μm, which is much smaller than the skin depth (170μm) at the switching frequency (200kHz) and much smaller than the width of PCB trace (2.75mm for HV winding and 6mm for LV winding). As a result, it is more important to equally distribute current along the radius of PCB winding to reduced the ac resistance. Considering of the ac winding resistance, the interleaved winding structure is the better than the non-interleaved option with smaller MMF, proper flux distribution and lower ac resistance.

TABLE I
PARAMETERS OF THE LEGO-MIMO PROTOTYPE

Specifications & Symbol	Description
HV Bus Voltage V_H	72V
HV Winding Turns N_H	8
HV Branch Inductor L_H	Coilcraft XEL6060 – 2.7μH
HV Blocking Capacitor C_H	200μF
HV Switch	GS61004B 100V
LV BUS Voltage V_L	9V
LV Winding Turns N_L	1
LV Branch Inductor L_L	Coilcraft SLC7530S – 64nH
LV Blocking Capacitor C_L	440μF
LV DrMOS	SIC632 24V
Switching Frequency f_s	200kHz
Transformer Core	0P4413UC, $\mu_r = 2500$

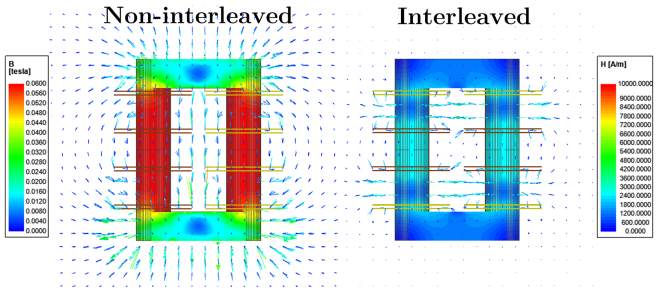

Fig. 10. 3D FEM simulation of the magnetic field strength and core flux density in the interleaved and non-interleaved winding structures.

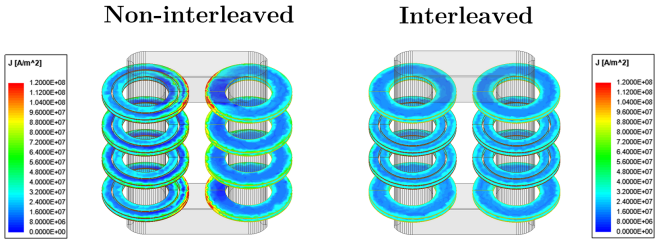

Fig. 11. 3D FEM simulation of the current density in the PCB windings of the interleaved and non-interleaved winding structures.

We use FEM to verify the magnetic analysis. The relative permeability of the core is 2500. The excitation current is 4A on the primary side and 16A on the secondary side. The excitation frequency is 200kHz. The magnetic field strength H in the window area and core flux density B are shown in Fig. 10. The magnetic field strength with non-interleaved structure is much stronger than the field strength in the interleaved structure. The distribution of H also matches the flux distribution analysis. The flux density in the core of the non-interleaved structure is significantly higher than that in the interleaved structure, especially on the two vertical sides. Fig. 11 shows the current density in the PCB windings. The outer edge of the PCB winding in the non-interleaved structure has higher current density due to the eddy current induced by the vertical flux, which matches the theoretical analysis and the FEM simulation in Fig. 10. The simulated winding loss in the interleaved structure is only 56% of the winding loss in the non-interleaved structure.

TABLE II
EQUIVALENT INDUCTANCE LINKING TWO WINDINGS IN THE CANTILEVER MODEL

	HV1	HV2	HV3	HV4	LV1	LV2	LV3	LV4	LV5	LV6	LV7	LV8
HV1	1.42mH	96.16nH	19.69μH	1.09μH	698.9nH	109.2nH	2.54μH	3.67μH	2.99μH	6.13μH	-9.89μH	23.02μH
HV2		1.42mH	1.09μH	19.69μH	3.67μH	2.54μH	109.2nH	698.6nH	23.05μH	-9.89μH	6.13μH	2.99μH
HV3			1.42mH	96.17nH	23.04μH	-9.89μH	6.13μH	2.99μH	3.67μH	2.54μH	109.2nH	699.3nH
HV4				1.42mH	2.99μH	6.13μH	-9.89μH	23.03μH	699.05nH	109.19nH	2.54μH	3.67μH
LV1					23.2μH	12.52nH	13.6μH	11μH	666.09nH	1.71μH	106μH	19.2μH
LV2						38.3μH	10.36μH	13.6μH	1.71μH	2.5μH	-31.5μH	106μH
LV3							38.3μH	12.52nH	106μH	-31.5μH	2.5μH	1.71μH
LV4								23.2μH	19.2μH	106μH	1.71μH	666.23nH
LV5									23.2μH	12.52nH	13.6μH	11μH
LV6										38.3μH	10.36μH	13.6μH
LV7											38.3μH	12.52nH
LV8												23.2μH

Another challenge in the multi-winding transformer design is to maintain voltage balancing and current sharing among the series or parallel connected LEGO bricks. Since all the parallel-connected and series-connected LEGO bricks are controlled by the same group of gate drive signals, active balancing control of each brick is not applicable. The voltage balancing and current sharing among the LEGO bricks are determined by the symmetry of the impedance matrix. A symmetric impedance matrix would enable passive voltage balancing and current sharing. As a result, the geometry and the winding structure of the magnetic structure should be carefully designed to achieve the highest level of symmetry among the LEGO bricks.

Table II listed the equivalent linkage inductance linking two windings in the interleaved magnetic structure as shown in Fig. 9. The data labeled in yellow is the grounding inductance. The equivalent linkage inductance is related to the "magnetic distance" between two brick windings. Take LV1 as the example, the linkage inductance between LV1 and LV2 is low and the inductance between LV1 and LV7 is high. Power tends to flow between windings that are physically closer to each other (due to the smaller linkage inductance). Suppose all the HV bricks and all the LV bricks are respectively controlled by two group of gate drive signals. The power processed by the i^{th} brick is determined by the linkage inductance that this brick is connected to: $\sum_{j\neq i} 1/(L_{ij}+L_i/N_i^2+L_j/N_j^2)$. Fig. 12 illustrates the power distribution in the HV and LV bricks. All HV bricks are connected in series, and all LV bricks are connected in parallel.

The power processed by the HV bricks in the interleaved winding structure is well balanced due to the symmetric winding structure of HV1 to HV4 (and a highly uniform impedance matrix, e.g., the inductance between HV1 and LV5 equals to the inductance between HV2 and LV8). The power distribution in the HV bricks with the non-interleaved winding structure is highly unbalanced due to the asymmetric winding structure. The total power that a non-interleaved structure can transfer from one port to another with the same phase-shift is significantly lower than that in an interleaved structure. The non-interleaved structure has higher equivalent linkage inductance among windings, which enhances the control resolution but limits the maximum power that can be transferred from port to port.

The power processed by the LV bricks is non-uniform in both cases due to the asymmetric LV winding structures (e.g., for the interleaved structure, LV1 and LV2 are still asymmetric and have different inductance matrix parameters).

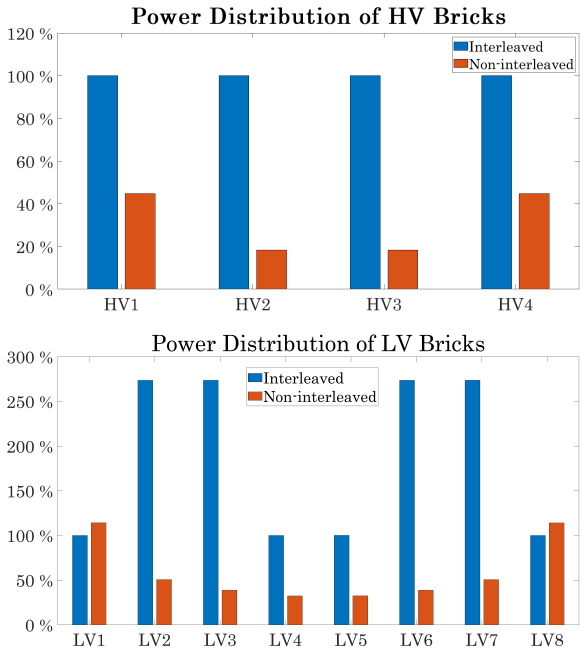

Fig. 12. Power distribution among the HV bricks and LV bricks. All the HV bricks work as one group with the same phase-shift angle. All the LV bricks work as another group with the same phase-shift angle.

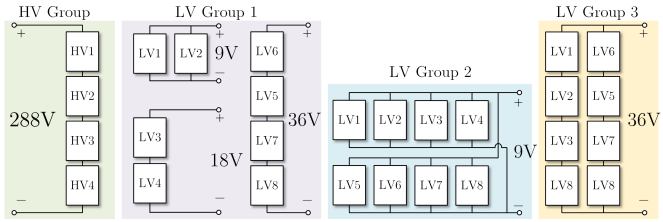

Fig. 13. Configurations of the HV/LV bricks in the LEGO-MIMO prototype.

Furthermore, the LV PCB boards in the interleaved structure are symmetric and the power of the two LV bricks placed on the same PCB in the interleaved structure is equal to each other ($P_{LV1}+P_{LV2}=P_{LV3}+P_{LV4}=\cdots$). Note this power distribution analysis is based on the assumption that the same phase-shift is applied to all HV bricks and all LV bricks. The parasitic components and the impedance of PCB traces and vias are neglected, which may offset the power imbalance. If significant external inductance are included in the system, the structural asymmetry caused by the multi-winding magnetics can be eliminated.

V. EXPERIMENTAL VERIFICATION

Fig. 13 shows a few different ways of configuring the LEGO bricks with four HV bricks and eight LV bricks. Each HV brick can block 72V and carry 2 A (dc). Each LV brick can block 9V and carry 7 A (dc). Four HV bricks are connected in series to interface with a 288V/2A dc bus. Two LV bricks (LV1 and LV2) are connected in parallel to support a 9V bus with 14 A of current. LV3 and LV4 are series-connected as a 18V/7A port and LV5–LV8 are connected in series as a 36V/7A port.

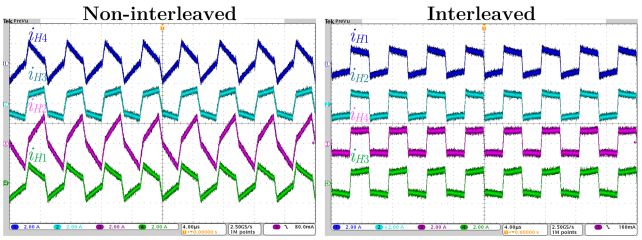

Fig. 14. Measured inductor currents in the four HV bricks at output power of 300W with interleaved and non-interleaved winding structures. The HV Group is the input port and the LV Group 1 (Fig. 13) are the output ports.

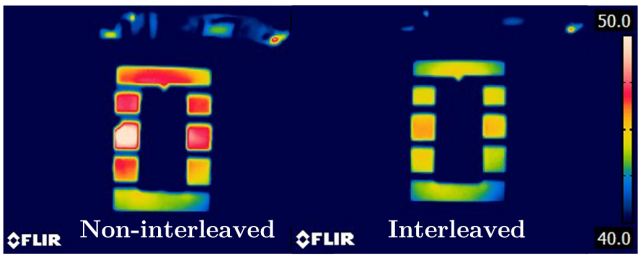

Fig. 15. Thermal images of the core with the interleaved and non-interleaved structures. The output power is 80W. The ambient temperature is 20°C.

They can also be reconfigured into a high power 9V/56A port and a high power 36V/14A port.

Fig. 14 shows the branch inductor current of four HV bricks with 288V input and 9V-18V-36V output. The current waveforms are all in phase because all the HV bricks are controlled by synchronized gate drive signals. The current of the HV bricks in the interleaved winding structure are more like an ideal trapezoidal waveform than the current in non-interleaved structure.

Fig. 15 shows the thermal images of the magnetic core with the interleaved and non-interleaved winding structures. The thermal images are captured by a thermography camera (FLIR E6) after the converter running for 8 minutes with output power of 80W. The ambient temperature is 20°C with no air cooling. The interleaved winding structure has lower core temperature due to the lower magnetic field strength. The hottest spot is 51.7°C in the non-interleaved structure and is 45.1°C in the interleaved structure.

Fig. 16 shows the measured efficiency of the LEGO-MIMO converter with the interleaved and non-interleaved winding structures. The interleaved winding structure offers higher system efficiency and higher power rating. The peak system efficiency is 96%. The maximum power that the system can deliver is 500W. All the LV bricks are controlled by the same phase-shift angle. The interleaved structure has higher efficiency due to the balanced power distribution and lower current amplitude. Since the 36V port has 4 LV bricks and both 9V port and 18V port have 2 LV bricks, the power processed by the 9V port, 18V port and 36V port are proportional to the brick number of each port: $P_{36V} = \sum_{i=5,6,7,8} P_{LVi} = P_{9V} + P_{18V}$. In the interleaved winding structure, $P_{9V} = P_{LV1} + P_{LV2} = P_{18V} = P_{LV3} + P_{LV4}$. Fig. 17 shows the measured port power in the two cases. In the non-interleaved structure, the power processed by the

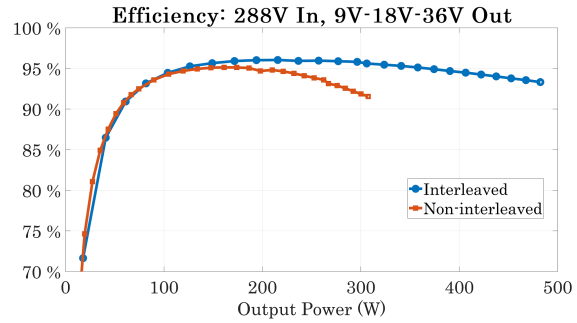

Fig. 16. Measured efficiency of the LEGO-MIMO prototype with two winding structures. The output ports are configured into 9V, 18V and 36V (Fig. 13).

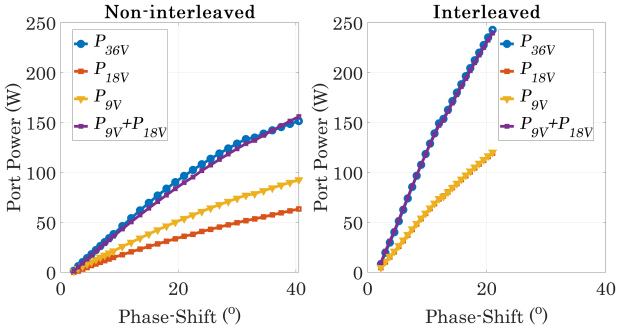

Fig. 17. The measured power of the 9V, 18V and 36V ports. Unbalanced power exists in the non-interleaved structure. Power is well distributed in the interleaved structure.

9V port ($P_{LV1} + P_{LV2}$) is higher than the power processed by the 18V port ($P_{LV3} + P_{LV4}$), which matches with the theoretical analysis presented in Fig. 12. With interleaved winding structure, the power of all the three ports are well balanced and evenly divided. The experiment results of port power also show that the two winding structures have different "power resolution" with the same phase-shift angle.

The experimental results verified that the LEGO-MIMO architecture is linearly extendable if the magnetic winding structure is symmetric enough. The number of HV and LV bricks can be further extended to cover wider input/output voltage and current ratings.

Fig. 18 shows the measured inductor current waveforms of four LV LEGO bricks with the three output groups configured as in Fig. 13. In LV Group 1, the bus voltages of LV Brick 1 and 2 are clamped to the port voltage and regulated to 9V. The voltage of the 18V port and the 36V port are regulated, but the voltage of each individual brick is not regulated. The voltage of LV Brick 3–8 is still unbalanced, causing unbalanced current slopes and higher inductor current magnitudes in i_{L4}, i_{L5}, i_{L7}. In the case of LV Group 2, all the LV bricks are parallel-connected and all their bus voltages are regulated. The inductor current waveform shows better current sharing. The current waveform is highly trapezoidal with low amplitude. In LV Group 3, voltage unbalancing still exists among the LV bricks since none of them are individually regulated.

Fig. 19 compares the efficiency of the three output port configurations. LV Group 2 achieves the highest efficiency especially with higher output power. The reasons are the

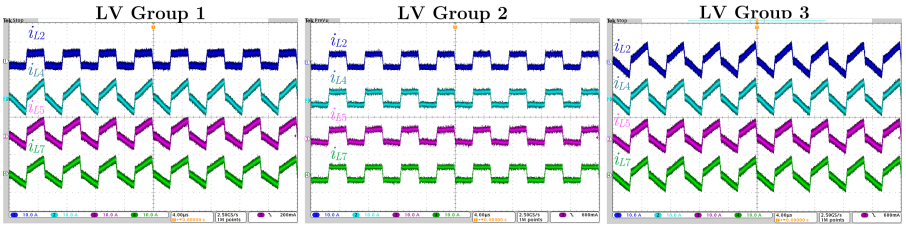

Fig. 18. Measured inductor current of the four LV bricks at output power of 300W with interleaved winding structure. HV Group is the input port, LV Group 1, LV Group 2 and LV Group 3 are the three output configurations.

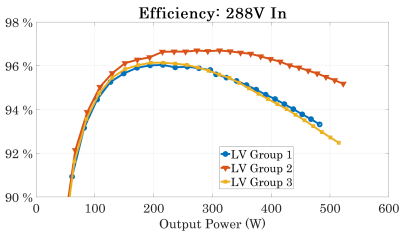

Fig. 19. Measured efficiency of the three output port configurations. LV Group 2 achieved the highest efficiency due to the highest symmetry.

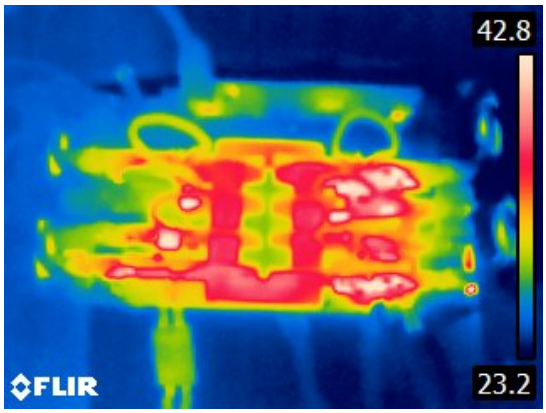

Fig. 20. Thermal image of the LEGO-MIMO converter with $P_o = 500$W. The output ports are configured as LV Group 1. The airflow is 21.9 CFM from left to right with 23°C ambient temperature.

well balanced port voltage and better current distribution. The maximum efficiency of LV Group 2 is 96.7% with an output power of 300W. LV Group 3 has the lowest efficiency because all the LV inductors currents have high peak amplitude.

Fig. 20 shows the thermal image of the LEGO-MIMO converter when it is configured as LV Group 1. The graph is captured after 20 minutes operating with an output power of 500W. A left to right 21.9CFM air flow is applied. The temperature of the prototype is below 45°C. The hottest components are the HV inductors and the LV DrMOS. Since power is processed in a distributed manner in the LEGO-MIMO architecture, heat is naturally distributed and no additional heat sink is needed, which helps to improve the power density.

VI. Conclusions

This paper presents a LEGO-MIMO architecture for multi-port ac-coupled power converters. The LEGO-MIMO architecture has simple control interface, reconfigurable input/output capability and linear extendable port voltage and power ratings. We performed power flow analysis on the multi-winding transformer, and developed a four-port prototype with 12 LEGO bricks to verify the effectiveness and functionality of the LEGO-MIMO architecture. The multi-winding magnetic structure is investigated and optimized to guarantee higher efficiency and better power balancing. A matrix conversion method is proposed to simplify the power flow control for the LEGO-MIMO system. The effectiveness of the LEGO-MIMO concept is verified by experimental results.

Acknowledgment

The authors would like to thank DOE ARPA-E CIRCUIT program and the Princeton E-ffiliates for supporting this work.

References

[1] A. K. Bhattacharjee, N. Kutkut and I. Batarseh, "Review of Multiport Converters for Solar and Energy Storage Integration," in *IEEE Transactions on Power Electronics*, vol. 34, no. 2, pp. 1431-1445, Feb. 2019.

[2] S. Qin, S. T. Cady, A. D. Domínguez-García and R. C. N. Pilawa-Podgurski, "A Distributed Approach to Maximum Power Point Tracking for Photovoltaic Submodule Differential Power Processing," in *IEEE Transactions on Power Electronics*, vol. 30, no. 4, pp. 2024-2040, April 2015.

[3] H. Wang, D. Xu, B. Xu, H. Li and Y. Zhu, "A Dual-Energy-Source Uninterruptible Power Supply (UPS)," *2018 International Power Electronics Conference (IPEC-Niigata 2018 -ECCE Asia)*, Niigata, 2018, pp. 2270-2277.

[4] Z. Zhang, H. Gui, D. Gu, Y. Yang and X. Ren, "A Hierarchical Active Balancing Architecture for Lithium-Ion Batteries," in *IEEE Transactions on Power Electronics*, vol. 32, no. 4, pp. 2757-2768, April 2017.

[5] P. Wang, Y. Chen, Y. Elasser and M. Chen, "Small Signal Model for Very-Large-Scale Multi-Active-Bridge Differential Power Processing (MAB-DPP) Architecture," *2019 IEEE 20th Workshop on Control and Modeling for Power Electronics (COMPEL)*, Toronto, 2019, pp. 1-8.

[6] C. Zhao, S. D. Round and J. W. Kolar, "An Isolated Three-Port Bidirectional DC-DC Converter With Decoupled Power Flow Management," in *IEEE Transactions on Power Electronics*, vol. 23, no. 5, pp. 2443-2453, Sept. 2008.

[7] C. Fei, F. C. Lee and Q. Li, "High-efficiency high-power-density 380V/12V DC/DC converter with a novel matrix transformer," *2017 IEEE Applied Power Electronics Conference and Exposition (APEC)*, Tampa, FL, 2017, pp. 2428-2435.

[8] G. C. Knabben, J. Schäfer, L. Peluso, J. W. Kolar, M. J. Kasper and G. Deboy, "New PCB Winding 'Snake-Core' Matrix Transformer for Ultra-Compact Wide DC Input Voltage Range Hybrid B+DCM Resonant Server Power Supply," *IEEE International Power Electronics and Application Conference and Exposition (PEAC)*, Shenzhen, China, 2018, pp. 1-6.

[9] T. Ericsen, N. Hingorani and Y. Khersonsky, "Power electronics and future marine electrical systems," in *IEEE Transactions on Industry Applications*, vol. 42, no. 1, pp. 155-163, Jan.-Feb. 2006.

[10] R. W. Erickson and D. Maksimovic, "A multiple-winding magnetics model having directly measurable parameters," *PESC 98 Record. 29th Annual IEEE Power Electronics Specialists Conference (Cat. No.98CH36196)*, Fukuoka, 1998, pp. 1472-1478 vol.2.

[11] Y. Chen, P. Wang, H. Li and M. Chen, "Power Flow Control in Multi-Active-Bridge Converters: Theories and Applications," *2019 IEEE Applied Power Electronics Conference and Exposition (APEC)*, Anaheim, CA, USA, 2019, pp. 1500-1507.